Actuated Hybrid Mirrors for Space Telescopes

Gregory Hickey[a], [b], Mark Ealey[c], David Redding[1a]
[a]Jet Propulsion Laboratory, California Institute of Technology, Pasadena CA 91109;
[b]Lawrence Livermore National Laboratory, Livermore CA;
[c]Northrop Grumman Xinetics, Devens MA

ABSTRACT

This paper describes new, large, ultra-lightweight, replicated, actively controlled mirrors, for use in space telescopes. These mirrors utilize SiC substrates, with embedded solid-state actuators, bonded to Nanolaminate metal foil reflective surfaces. Called Actuated Hybrid Mirrors (AHMs), they use replication techniques for high optical quality as well as rapid, low cost manufacturing. They enable an Active Optics space telescope architecture that uses periodic image-based wavefront sensing and control to assure diffraction-limited performance, while relaxing optical system fabrication, integration and test requirements. The proposed *International Space Station Observatory* seeks to demonstrate this architecture in space.

Keywords: Active optics, space telescopes, nanolaminates, silicon carbide, wavefront sensing, wavefront control

1. ACTIVE OPTICS

The Hubble Space Telescope has been astoundingly successful, more than fulfilling the scientific ambitions of its progenitors – but only after its initial poor wavefront quality was corrected by enormously costly astronaut servicing.[1] Other space telescopes have had wavefront errors that could not be repaired, for instance the Deep Impact mission, which was severely defocused after launch.[2] Hubble's errors came in spite of its expensive, exquisitely polished, massive primary mirror, and its highly stable, massive composite structures. It came about through a test equipment failure, which went unrecognized due to the lack of a system end-to-end test.

Future space telescopes can be made tolerant of the sort of errors that Hubble and other missions have experienced, through the use of Active Optics: mirrors that are capable of adjusting their shape after launch, to correct for large figure errors, misalignments, testing errors, and other degrading effects; and the Wavefront Sensing and Control systems that command them. Active Optics *reduce the risk* that an unrecognized problem can cause a mission to fail.

Active Optics can also *reduce the cost* of space telescope missions. Active Optics are much lighter weight than conventional optics, allowing system-wide mass savings that convert directly to cost savings. Active Optics provide a high level of adjustability, relaxing fabrication tolerances, and allowing assembly to mechanical tolerances rather than optical tolerances. Active Optics can compensate for unanticipated environmental effects, such as misprediction of the thermal environment. Active Optics can compensate for the effects of gravity, making it possible to test telescope performance *to spec* during assembly and after integration. Telescopes designed to exploit these features will be less costly, require less time to integrate and test, and have a higher likelihood of meeting performance requirements than traditional telescopes.

This paper describes *Actuated Hybrid Mirrors* (AHMs), and associated Wavefront Sensing and Control (WFS&C) methods, which were developed by our team to provide Active Optics for space telescopes. AHMs are large mirrors, suitable for use as the Primary Mirror (PM) of a medium-sized telescope, or as the segments in a large, segmented PM. AHMs are hybrid structures, integrating a precision-replicated Nanolaminate foil facesheet, with a Silicon Carbide (SiC) substrate equipped with embedded electroactive ceramic actuators (Figure 1). Voltages applied to these actuators cause them to precisely bend the mirror for wavefront control. The voltage commands are determined by a WFS&C system that uses image-based phase retrieval techniques for high accuracy and resolution.

The Nanolaminate facesheets are formed by a magnetron sputtering process developed at Lawrence Livermore National Laboratory (LLNL)[3], and summarized in the next Section of this paper. Nanolaminate foils are formed atom-by-atom:

[1] david.c.redding@jpl.nasa.gov

first depositing a carbon separation layer; then a layer that will form the outer surface of the mirror, such as gold; then alternating layers of a crystalline metallic such as zirconium, and an amorphous layer such as Zr/Cu, which is created by depositing a thinner copper layer on the much thicker zirconium layer. Many hundreds of these alternating layers are deposited in the course of up to several days to create foils 10-100 microns thick.

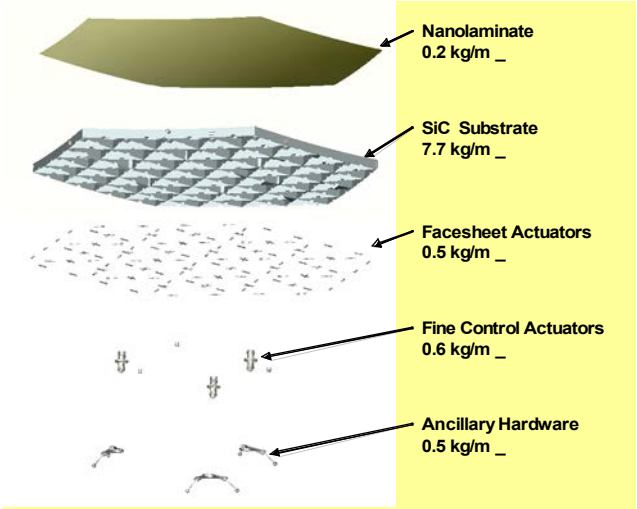

Figure 1. Actuated Hybrid Mirror.

Nanolaminates are deposited on nano-clean, super-polished glass or metal mandrels, which are figured to closely match the reverse of the desired optical figure – a convex mandrel for a concave optic. The first nanolaminate layers, which are deposited onto the parting layers, ultimately provide the outer mirror surface. These first layers are typically made using reflective materials such as gold; alternatively a reflective coating can be deposited after bonding of the nanolaminate to its SiC substrate and separation of the nanolaminate/SiC structure from the mandrel to form a free-standing optic.

The SiC substrates are made using the Ceraform process developed by Northrop Grumman Xinetics[4] and reviewed in Section 3. The substrates are carefully engineered for light weight, toughness, and for effective, smooth optical actuation. Embedded in the substrates are electrostrictive ceramic actuators, also developed by NGX, that are oriented parallel to the surface of the mirror. These are very low hysteresis, low creep devices. They have both global and local influence, which provides both high WFS&C control authority and high control precision.

AHMs are integrated in a robotic bonding process, with the substrate being bonded directly to the nanolaminate facesheet while the latter is attached to the mandrel. Careful control of bonding pressures is required to keep the glue line uniform and to minimize frozen stresses. When cured, the bonded mirror is lifted to separate the nanolaminate from the mandrel. The actuators are bonded into place; the mirror is tested, and then integrated into the telescope.

Operation of a telescope with an AHM primary requires the ability to measure the total system WFE, and then to compute and implement new actuator settings to compensate the WFE. This WFS&C process can be done with minimal complexity and expense, by using the science imaging camera itself as a Wavefront Sensor (WFS), as described in Section 5. To measure the WF, the spacecraft is pointed at a bright, isolated star, and in- and out-of-focus images are recorded. These focus-diverse images are downlinked to the ground for computer processing, using the JPL Modified Gerchberg-Saxton (MGS) Phase Retrieval software. The MGS software processes the defocused image data to produce a map of WF errors. From this data, and knowing the precise influence of each actuator based on initial calibration measurements, it is straightforward to compute new voltages for each actuator that correct the WFE. These voltages are uplinked to the spacecraft and implemented, completing one correction cycle.

The initial WFS&C correction following launch of a spacecraft can be expected to be quite large, 2-20 microns RMS, due to gravity release, fabrication errors, testing errors, alignment shifts incurred during launch, and misprediction of the thermal environment. These effects can be easily compensated, however, leaving residual, post-control WFE that meet mission requirements: meter-class AHMs have demonstrated post-WFS&C performance traceable to system-wide WFE of less than 50 nm RMS.

Subsequent WFS&C corrections will be much smaller and infrequent. For telescopes in a static thermal environment, or for which active PM thermal control is provided, updates are expected to be required only once every 3-7 days. This level of WFS&C operations will not interfere with normal operations of an astronomical telescope in any significant way.

NASA (JPL and JSC) and the Space Telescope Science Institute are proposing space demonstration of this Active Optics architecture on the International Space Station (ISS).[6] The International Space Station Observatory (ISSO) will utilize an existing 50 cm AHM as the primary for a telescope mounted on gimbals and attached to the ISS, to provide images of the earth and astronomical objects.

2. ACTIVE OPTICS

Magnetron sputtering is a process whereby a substrate – such as a super-polished glass mandrel – can be coated atom by atom with materials, such as gold, copper, zirconium, or carbon. Sputtering is a vacuum based process implemented at a low argon gas pressure of ≈ 2 to 4 mill-torr. A target, consisting of a bar of the material to be deposited, is raised to a high negative voltage by a DC power supply. This attracts Ar+ ions, which impact the target at energies typically in the range of 300 to 700 eV. These atomic collisions eject atoms from the sputter target as well as energetic secondary electrons. The ejected atoms form a ballistic atom cloud that impinges on the mandrel surface, forming a film by condensation on the mandrel surface. The secondary electrons are trapped in the magnetic field of the magnetron sputter source, where they act to further ionize the argon gas, sustaining the plasma and the sputtering rate.

The coating rate can be reproducibly varied and defined by operating the DC power supply in the Power control mode, by the physical distance of the mandrel from the sputter target, by the pressure of the argon gas, and by the rate of motion of the mandrel through the atom flux from the source. The coating rate affects the internal stresses of the coating, as more energetic depositing atoms can displace atoms within the coating, increasing the residual stress. The optimization of these parameters – and their stability – is important in achieving uniform, low residual stress nanolaminates.

Nanolaminates are thick multilayer coatings formed by alternating coating materials in the same coating run, using multiple sputter source targets made of differing materials.[7]-[10] Each target is energized for a specific deposition period, before switching to the next target, to create multilayer structures with many hundreds of nanometer-thick layers, and overall thickness of tens of microns. Uniformity of deposition is provided by continuous translation and rotation motion of the substrate under each sputter deposition source.

Nanolaminate materials are nanometer layered, low-contamination solids with high interface concentration. The individual nanolaminate component material layers can be crystalline/crystalline,[11] amorphous/crystalline[12] or amorphous/amorphous in structure. [13] The layers can be elemental, alloy, or in the form of compounds to produce a rich variety of metal-oxide, oxide-oxide and metal-metal structures. Multilayers have been synthesized from more than 75 of the 92 naturally occurring elements, and applied in a broad range of scientific investigations and technological development efforts. Individual layer thicknesses of less than 1.0 nm have been achieved[14],[15] and total thicknesses from less than 10 to more than 400 microns have been made with several materials.

The different materials used in AHM nanolaminates have different functions. The first material deposited on the mandrel is typically a few Å of pure carbon, to form a release layer. Then an optical outer surface is deposited, such as gold. This can form the reflecting outer surface of the finished AHM mirror – or it can be overcoated with a different optical coating after the AHM mirror is bonded to the SiC actuation structure and separated from the mandrel. The major nanolaminate thickness is formed by alternating crystalline layers and amorphous layers: zirconium, which is crystalline, interleaved with Zr/Cu amorphous layers.

A transmission electron micrograph of a multiple period ZrC/Si multilayer developed for X-ray optics is shown in Figure 2. The interface quality as well as the layer uniformity is clearly demonstrated in this micrograph. Though the precision apparent here is not necessary for the AHM structures, the absence of structural defects that could lead to mechanical failure of the nanolaminate is required. This is achieved by a strong focus on the cleanliness of the mandrel surface, and by suppression and control of particle generation during deposition of the nanolaminate structure.

Nanolaminates for AHMs have been fabricated in the Very Large Optic Coater (VLOC) at Lawrence Livermore National Laboratory, as schematically shown in Figure 3, with a 1.5-meter diameter convex mandrel in the material deposition zone. The rectangular box on the top of the VLOC system houses four 5”x 63” sputter target magnetron deposition sources: one for carbon, one for gold, one for copper and one for zirconium. Mandrel substrates are coated

with a layer of a nanolaminate as it passes in front of an energized, down-facing sputter source, for a specified period of time. After deposition of this layer, the source is de-energized and rotated to another position. The next material is deposited by energizing the next downward facing source, and passing the mandrel substrate through its atom flux. The total time required to deposit a 21 micron thick nanolaminate, after reaching a initial vacuum pressure of 5 x 10^{-7} torr, is 40 hours. This nanolaminate will contain 446 periods, each period consisting of a deposited 43.5 nm thick zirconium layers and a 3.5 nm thick copper layers. The resulting foil is 93% Zr and 7% Cu by volume. It has a Young's Modulus of 68-70 GPa, a Poisson's ration of 0.34, and a Biaxial Modulus of 101-104 GPa. Thermal Expansion is 6.4 ±0.3 ppm/C.

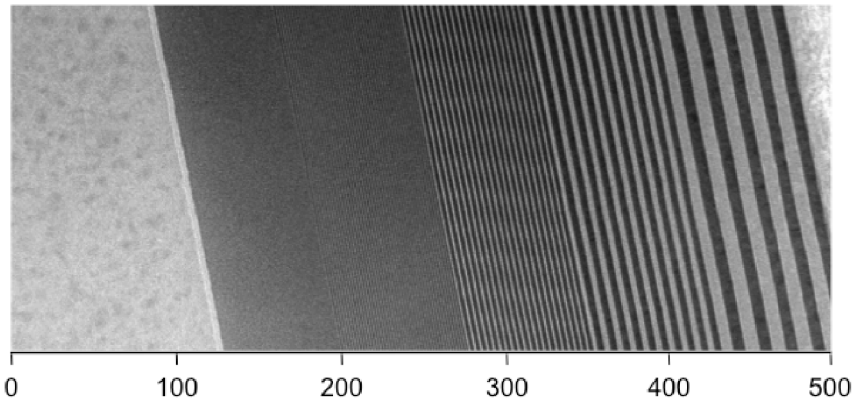

Figure 2. A transmission electron micrograph of a multiple period ZrC/Si multilayer developed for X-ray optics is shown. The thinnest layers deposited in this structure were 0.4 nm thick; the thickest were about 32 nm thick.

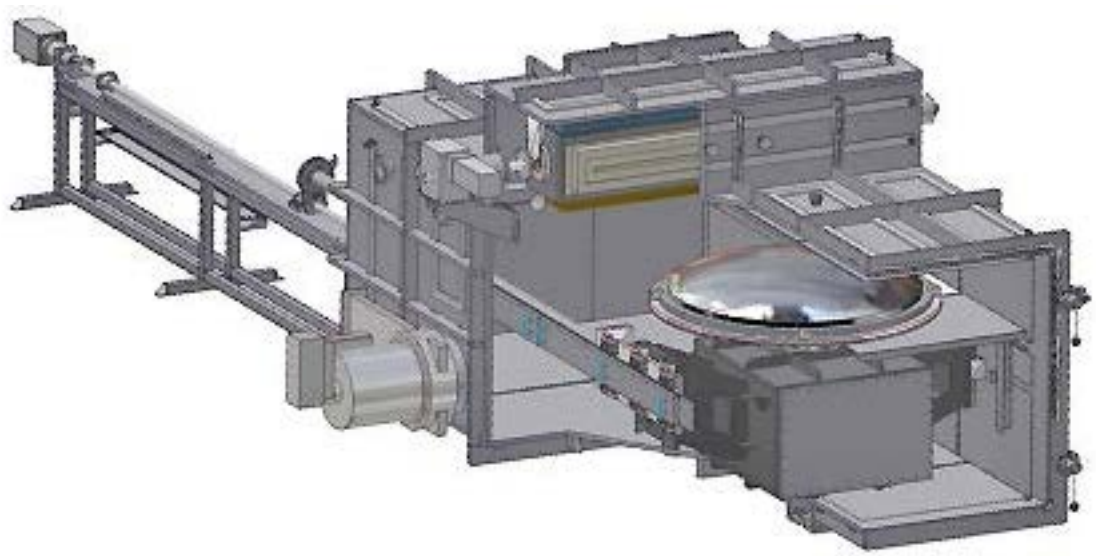

Figure 3. A cut-away drawing of the Very Large Optic Coater (VLOC) at Lawrence Livermore National Laboratory, showing a convex mandrel mounted in the deposition chamber, below the box holding the 4 magnetron sputter deposition sources.

The argon plasma in front of one of the 5"x63" rectangular magnetron sputter sources is shown in Figure 4. The plasma is seen as two white linear zones, and a mandrel rotating at 25 rpm is shown initiating its pass under the magnetron source, during which a zirconium layer was deposited. The finished 21 micron thick nanolaminate is shown on its 152 cm diameter Zerodur mandrel in 0. The outer surface is a zirconium layer.

Achieving uniform, low-stress, high repeatability, rapid nanolaminate fabrication has required systematic refinement of the magnetron sputter deposition process, based on careful engineering calibration of process parameters. Important nanolaminate structural and fabrication process characteristics include: 1) layer thicknesses; 2) layer thickness

uniformity throughout a sample; 3) layer composition; 4) fabrication process reproducibility; 5) fabrication process stability in a long (> 300 hours) deposition run; 6) fabrication process flexibility.

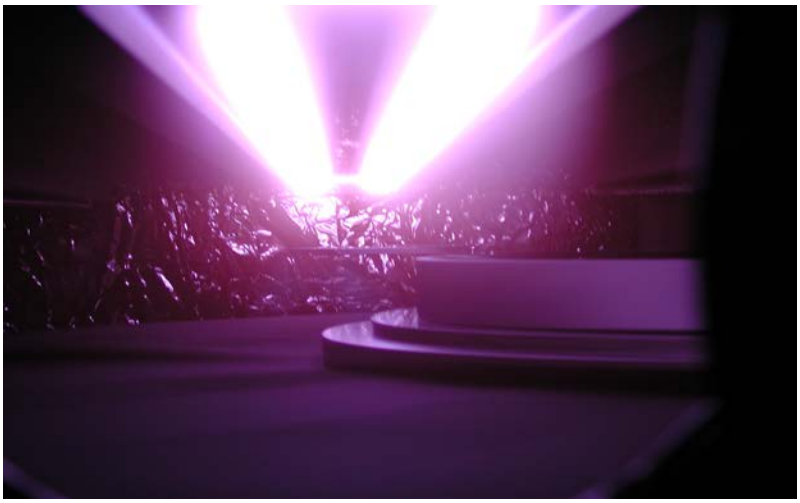

Figure 4. Argon plasma below the Zr 5"x63" rectangular magnetron sputter source in VLOC, one of 4 sources used in deposition of an AHM nanolaminate, with a mandrel, rotating at 25 rpm, initiating its pass.

Figure 5. A nanolaminate coated 152 cm diameter convex Zerodur mandrel shown during removal from the VLOC coating system. The surface shown is that of a 43.5 nm thick Zirconium layer.

The *optical* properties of a nanolaminate are largely a function of the optical quality of the mandrel on which it is deposited. The mandrel is a reusable tool, formed in the opposite shape of the desired finished optic (convex where a concave optic is desired). Mandrels can be made from metals, ceramics, or glass: ULE has been preferred for its low expansion properties and the ability to achieve surface roughness of < 5 Å. It is not necessary to achieve good optical figure: a low spatial-frequency error greater than 1 micron will easily be corrected by the actuators in the finished AHM with very little residual WFE. AHM optics fabricated using mandrels manufactured at the University of Arizona have demonstrated post-fabrication, post-WF control errors of less than 6 nm RMS.

3. SILICON CARBIDE MIRROR SUBSTRATE

AHM substrates are made from CERAFORM SiC, a material with outstanding stiffness, toughness, and thermal stability (key mechanical properties are listed in Figure 6). CERAFORM is a *reaction-bonded* form of SiC, originally developed by UTOS, Inc., and further developed by NGX. [7]

CERAFORM SiC parts begin as a "fugitive-core" mold, machined into a plastic foam material enclosed within a graphite case. A slip, or slurry, of SiC in nanopowder form is poured into the mold, and the part is then freeze-dried to extract the moisture from the slip. The plastic mold material is leached out, and then the part is fired into a green state, leaving the part in an easily-machined condition. The green part is inspected, and certain features, such as cutouts for the actuators, are milled into the part. A final, high temperature firing establishes full hardness of the part.

The final step in preparation of the substrate for bonding to the nanolaminate is a rough grinding of the front surface to match the curvature of the mandrel to within 25 um. This step uses a large computer-controlled grinder, using a coordinate measuring machine to measure the SiC surface. The objective is to keep the bond line small, which helps to limit stresses in the adhesive from impacting the final surface figure quality.

This fugitive-core process is well suited to high production volume, replicated manufacture of near net shape optical-quality parts. Molds are easily generated using computer-controlled milling machines. The finished part experiences only a predictable 1% shrinkage. The use of nanopowders in the slip permits complete flow into the mold, and yields a final part with a microstructure that can be polished to a sub-10-Angstrom finish, though this feature is not required for AHMs. Essentially, any part for which a mold can be created, can be formed.

Property	Units	Aluminum	Beryllium	SiC	ULE	Desire
ρ, Weight	g/cm3	2.71	1.85	2.95	2.21	Low
E, Stiffness	GPa	68.3	303	364	67.6	High
E/ρ,Specific Stiffness	KN-m/g	25	164	123	31	High
σ/ρ, Stress Loading	N-m/g	46	11	24	3.2	High
α,Thermal Soaks	ppm/°C	22.7	11.4	3.38	±0.03	Low
Δα Homogeneity	ppb/°C	100	100	30	10	Low
K/α, Thermal Gradients	MW/m	6.9	19	51	44	High
K/rCp,Thermal Diffusivity	m2/s	6.55	6.07	8.7	0.08	High
K/αE, Thermal Stress	MW-m/N	101	63	140	646	High

Figure 6. Properties of optical materials.

The process of designing AHM substrates is deterministic, using Finite-Element structural models of the mirror to optimize parameters such as cell width, facesheet thickness, height and thickness of main ribs, and the layout of minor or "cathedral" ribs, so as to achieve the required first mode frequency, areal density, and actuation performance. An example of a large AHM is shown in Figure 7, illustrating typical rib structure.

Figure 7. An AHM SiC substrate, seen from the back, showing rib structure.

A common AHM design trade is to optimize the number of actuators to be used, with more actuators yielding better control capability, but at the cost of minor additional mass. An example of such a trade for a large AHM is shown in Figure 8. Note that the correctability of most low-order optical aberrations ranges from 10x to 300x, depending on the particular aberration term and the number of actuators.

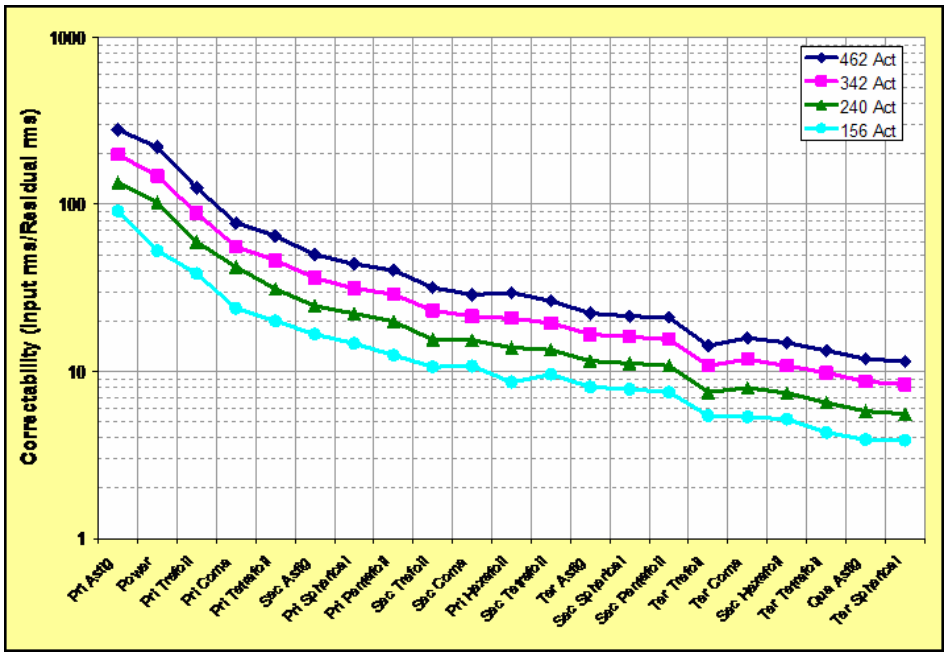

Figure 8. Correctability vs. number of actuators for a large AHM.

4. AHM INTEGRATION

Transfer bonding of the SiC substrate to the nanolaminate occurs with the nanolaminate foil still attached to the mandrel on which it was formed. Mounting inserts are installed into the silicon carbide substrate prior to bonding, so that the adhesive will fill any mount insert strain deformations. The adhesive is a filled aerospace epoxy with relatively low strain and thermal coefficient of expansion. The bonding is accomplished using a multi-axis robot, following a specific squeeze-out force profile that provides the good alignment and low internal stress. This force profile is specific to each different aspheric shape.

Initial bonding operations are conducted at room temperature to mitigate CTE induced the mandrel is separated from the nanolaminate in an environmental chamber, using normal forces applied locally and following a temperature profile designed to ensure that any fractures do not enter the glass mandrel, but rather follow the parting line between the mandrel and the nanolaminate. After separation, the Nanolaminate edges are trimmed using a short pulse laser, and the edges are sealed with a bead of epoxy. Subsequent processing is done at an elevated temperature to insure dimensional stability of the bond lines.

The next step in the AHM integration process is to bond the actuators into the mirror. Actuation of the AHMs utilizes Xinetics electrostrictive ceramic actuators, oriented in a surface-parallel configuration. These actuators are made using lead magnesium niobate (PMN) material impregnated into thin tapes, which are interleaved with platinum electrodes, stacked, and then fired at high temperature. The firing process places the Curie temperature of the finished actuator material well below the operating temperature, so that the actuators exhibit nearly purely electrostrictive behavior, with little or no creep, and hysteresis of 1% or less. After firing, each actuator is subjected to a low temperature, low voltage burn-in procedure to identify the best units. The actuators that pass this test are highly reliable, with essentially infinite life.

The actuators are first bonded to small interface tabs equipped with slots that fit into cutouts in the AHM ribs. Then the combined actuator/tab assemblies are bonded into the AHM. This bonding occurs with the actuators powered to half

their operating voltage, so thay are at half extension when the mirror is at its unstressed condition. This gives them the capability of contracting as well as expanding, so that they have both positive and negative WF control capability.

Each actuator is controlled via two wire leads, as indicated in Figure 9. These wires are routed to specific pick up points, where they are nested into strain relieved cable assemblies. These cables become the electrical interface for the mirror.

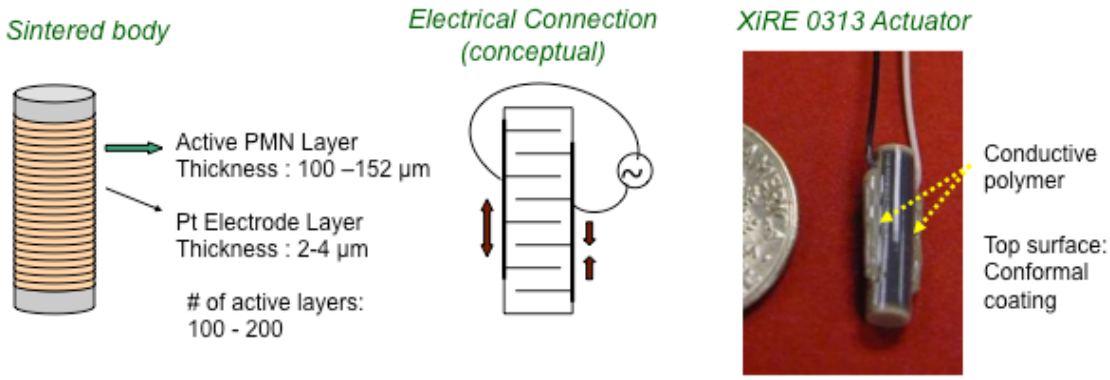

Figure 9. Northrop Grumman Xinetics XiRE electrostrictive actuator.

The final step in integration of AHM mirrors is attachment of mechanical hardware such as bipods, which are installed into the mount inserts to produce the mechanical interface. Other mechanical hardware, including any desired thermal control hardware, can also be installed at this point.

Functional testing, both electrical and mechanical, is conducted at various points during the integration and assembly process. Optical testing is conducted after release of the mirror from the mandrel, and after actuator installation. A typical finished mirror assembly, including solid state actuators, electrical wiring harness, and mechanical bipod mounts is shown in Figure 10.

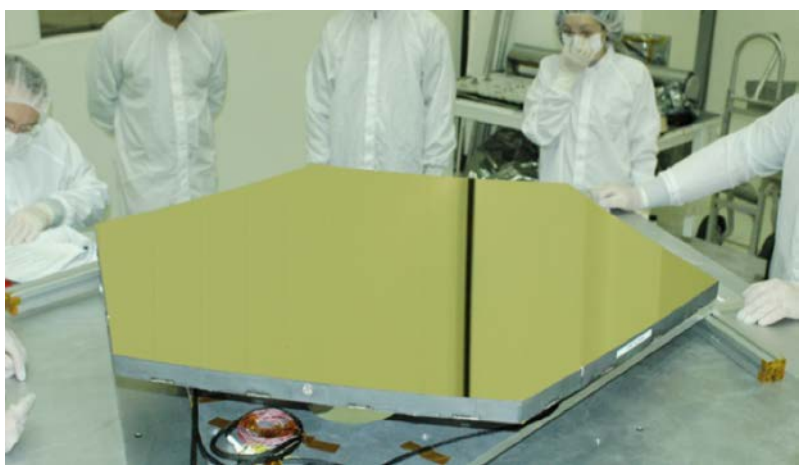

Figure 10. An AHM after integration.

5. WAVEFRONT SENSING AND CONTROL

Wavefront Sensing and Control for a space telescope equipped with a single-mirror, non-segmented, monolithic PM can be implemented with little increase in hardware complexity, compared to a conventional, passive telescope, as sketched in Figure 11. Telescopes with a segmented PM are more complex, as discussed in [5] and [17]. The conventional PM is replaced by the AHM primary, its cabling and low-voltage electronics drivers; the drivers are electronically connected to the telemetry system so that they can receive voltage commands. In general, the mass of the AHM primary and its electronics will be less than a conventional optic.

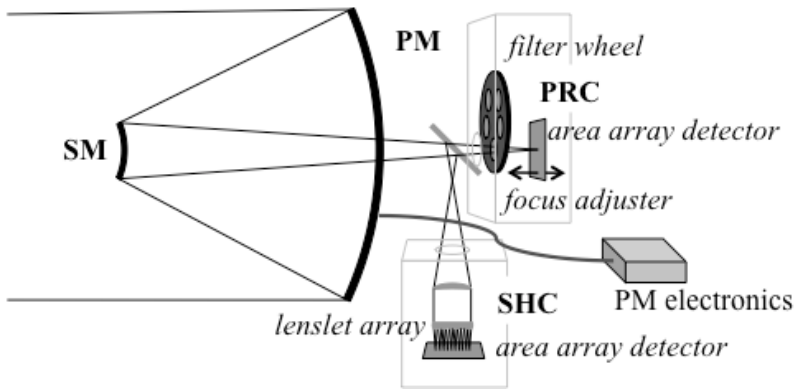

Figure 11. WFS&C elements.

Image-based WF sensing requires only hardware that is likely to be part of a science camera: an area array detector; a narrow-band filter in a filter wheel; a means for changing the telescope focus (by motion of the Secondary Mirror (SM) or Focal Plane Assembly (FPA)); and the ability to command these devices and receive images. As a stand-in for a space telescope science imaging camera, we have built portable *Phase Retrieval Cameras* (PRCs) that have these capabilities, and have used them successfully on numerous laboratory hardware testbeds and tests of large optics, including AHMs.**Error! Reference source not found.** In what follows, we will refer to the telescope imaging camera generically, as the "PRC."

The last WFS&C element is a Shack-Hartmann Camera (SHC) WFS.[18] The SHC is included because it has a larger WFE capture range than the PRC; it may also have an extended-scene WFS capability that could be used to monitor the WF during science observations.**Error! Reference source not found.** The SHC adds a second imaging detector, a pupil imaging lens, and a lenslet array to the typical space telescope instrument complement (Figure 11). The SHC is included in the plans for the ISSO as "insurance." As AHM technology matures, it may no longer be required. In what follows, we assume that the telescope has a SHC.

WFS&C for a space telescope such as ISSO will proceed in 2 phases. The first, *Initialization WFS&C* phase will occur when the telescope is safely on orbit, thoroughly checked out, and ready to begin observations. The telescope WF may be poor at this point, perhaps as much as several waves RMS. Initialization will begin with the telescope pointed at a bright, isolated guide star, and with the AHM voltages set at a uniform 50V – the minimum stress condition for the mirror.

The first Initialization step will be to record a star image in the SHC. The SHC uses a pupil imaging lens to place an image of the entrance pupil, typically located at the PM, onto the lenslet array. The lenslets create subaperture images – an array of spots – on the SHC imaging detector. When there is no wavefront error, the wavefront at the lenslet array will be flat, and the spot pattern will be a perfectly regular grid. Wavefront errors, however, will change the phase of the light at the lenslets, so that the WF seen in each subaperture will be tilted. This causes each spot on the SHC imaging detector to shift, by an amount proportional to the tilt in the corresponding subaperture, and the pattern of spots loses its regularity. Ground processing of the SHC image will quickly determine the WF that generated it, as well as the new actuator commands and focus adjustment mechanism settings needed to correct the WF. These are uplinked to the telescope, and the process is repeated until the WFE seen in the SHC is small.

Figure 12 shows the result of a laboratory experiment that simulates this process, using a SHC, a PRC, an autocollimating flat, and a deliberately aberrated AHM. A white light source coupled to an optical fiber simulated a star. The spot pattern produced by the (astigmatic) AHM is shown on the left side of the figure, with a blow-up in the center. The processed WF estimate is at the right of the figure. A few SHC iterations will generally reduce large initial WFE to under a quarter wave RMS, for handoff to the next step.

The second Initialization step is to use the PRC for image-based WFS, to produce a higher resolution, more accurate WFE map, based on multiple defocussed star images. Typically 4 images are recorded at 4 different focus settings: ±8 waves and ±6 waves provide a reasonable set, as illustrated in **Error! Reference source not found.**. These images will be downlinked for ground processing using the JPL-developed Modified Gerchberg-Saxton (MGS) phase retrieval software. This processing generates a WFE estimate and new actuator command values, which are uplinked to the

telescope and implemented. A few iterations of PRC-based control should be sufficient to achieve the required optical performance.

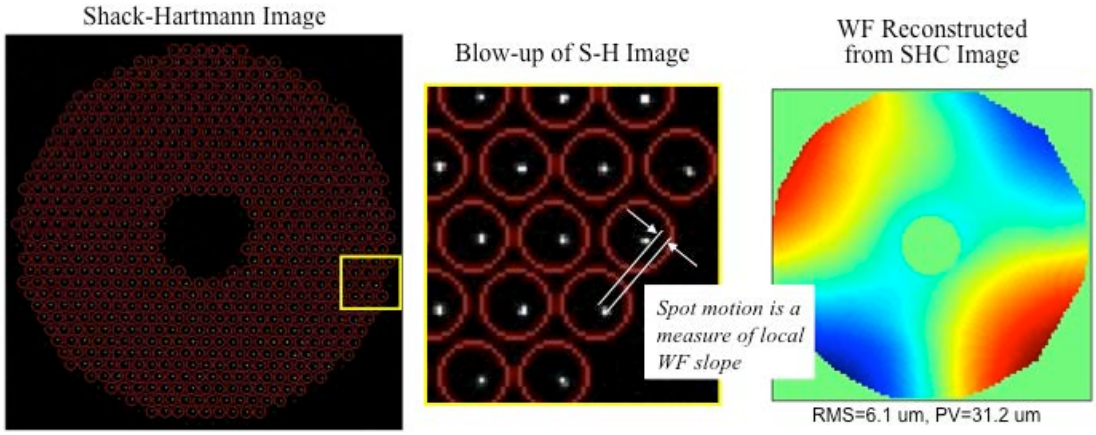

Figure 12. Shack-Hartmann image of a deliberately aberrated AHM, with reconstructed WF.

Image-based phase retrieval WFS was first propounded by Gerchberg and Saxton;[21] it received extensive further development during the Hubble recovery efforts in the early 1990s. Phase retrieval is an indirect method for determining the WF phase, exploiting the fact that the complex amplitude at the The JPL MGS software utilizes multiple parallel "inner loops," each processing a different single image, using an approach close to the original Gerchberg-Saxton algorithm. Defocussed images are used, as they show strong signatures of any optical aberrations. Following inner loop convergence, estimates from each image are mixed to form a joint estimate, which is used to restart the inner loops. Several cycles of this "outer loop" iteration drives the joint WF estimate to converge.

For large WFE cases, the phase exceeds 2π, causing phase wrapping, which must be resolved to provide phase estimates for control. The MGS software does this using phase unwrapping and an "adaptive prior:" a reference phase that is assumed to be part of the answer, but that is in fact evolved slowly through multiple outer-loop MGS iterations. As the solution evolves, phase wrapping is broken, and the iterating phase approaches null, where the algorithm is most accurate.

Figure 13 illustrates this process, concluding the same laboratory experiment. The defocussed images on the left of the figure were processed to produce the estimate on the right. The mirror test was run in autocollimation, with a large return flat in front of the mirror, so that the wavefront error (83 nm) is 2x worse than would be experienced in a telescope looking at an external source, such as a star. The equivalent single-pass WFE is 42 nm.

The MGS software has been utilized on a wide range of optics, both large and small. It was originally developed for the NASA Next Generation Space Telescope / James Webb Space Telescope, and was thoroughly proven using various JWST hardware testbeds and optics tests.REF Under the NASA Terrestrial Planet Finder project, wavefront sensing repeatability of l/10,000 was demonstrated using the High Contrast Imaging Testbed, a highly-stable, small optics testbed for exoplanet science.REF Capture range was shown to exceed 15l peak-to-valley on the Advanced Mirror System Demonstrator large cryogenic Be mirror segment.REF MGS is in routine operation at the Palomar Mountain Observatory, where it is used to calibrate the non-common path WFE between the SHC wavefront sensor and the IR science camera. MGS won NASA's Software of the Year award for 2007.

The second phase of WFSC operation is *WFS&C Maintenance*, which will occur occasionally throughout the mission. Maintenance phase will consist simply of periodic remeasuring of the WFE, using a guide star and the PRC. As in the Initialization phase, data will be recorded and downlinked for processing on the ground. New actuator commands are then uplinked for implementation on the mirror. The interval between Maintenance updates should be chosen so that the WFE does not drift out of specifications. Depending on particulars of the mission, this time should be from 1 to 7 days – a very low impact on science operations.

WFS provides another significant benefit – the ability to monitor imaging performance in detail, providing an excellent basis for predicting the Point Spread Function for any particular observation. This can be used in Image Restoration processing to improve the imagery.

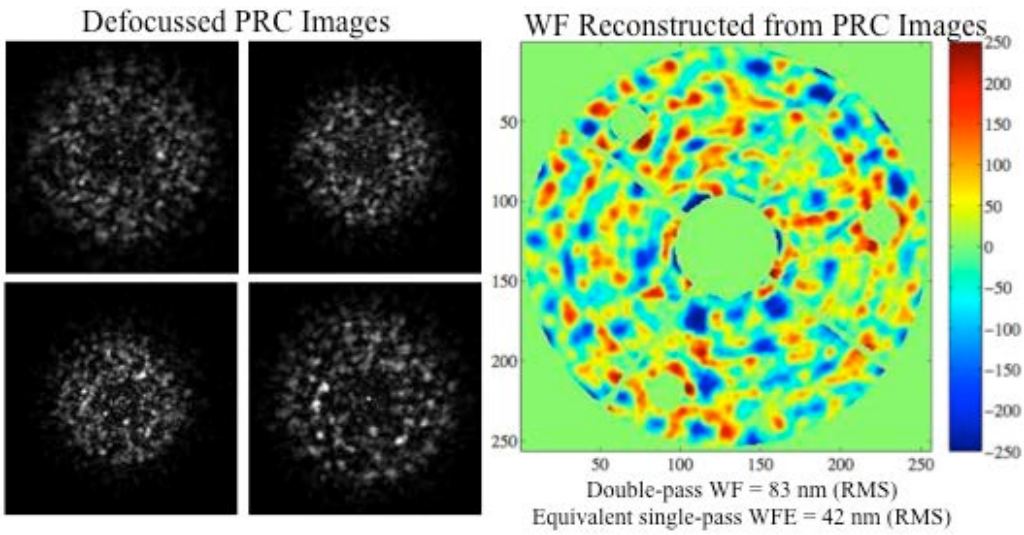

Figure 13. Example of PRC control, showing defocussed images (left) and the corresponding WF estimate (right).

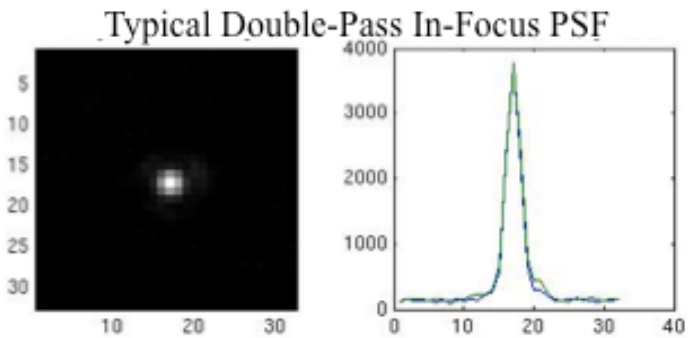

Figure 14. Example of an in-focus image (PSF) following completion of PRC control.

6. CONCLUSION

Active Optics using AHMs provide the ability to correct for large optical aberrations that might be incurred anywhere in the beam train, at any time during the fabrication or operation of the telescope, by factors of 10 to 300 (Figure 8). By correcting for the effects of gravity, AHMs permit testing of the telescope during assembly at the component, telescope-only, or fully integrated system levels, directly to the required performance specifications, reducing the risk of an undetected failure. AHMs can correct very large errors on orbit, reducing the risk that the launch or orbital environment would cause changes that degrade mission performance. These factors reduce mission risk.

A space telescope that is designed to exploit these capabilities can loosen fabrication and assembly tolerances, permitting (for instance) alignments to mechanical rather than optical tolerances for many components, speeding the Integration and Test phases of the mission. Very large cost savings come from the fact that AHM active mirrors are significantly lighter weight than other approaches. The use of replication techniques provides rapid, repeatable fabrication and reduced cost, especially where multiple copies of a particular mirror are required, either for multiple telescopes, multiple segments of a segmented mirror, or simply to provide spares. As shown in this paper, these advantages come without compromising optical quality.

The use of WF sensing as part of Active Optics provides useful knowledge of the optical system during operations. It can be used to monitor performance, and by providing detailed Point-Spread Functions, it enables accurate image restoration processing. In sum, Active Optics provide great potential for reducing the cost of high-performance space telescopes, a new paradigm that we hope will be demonstrated in space by the International Space Station Observatory.

This research was carried out at the Jet Propulsion Laboratory, California Institute of Technology, under contract with the National Aeronautics and Space Administration.

7. REFERENCES

[1] Hubble summary
[2] Deep Impact optical aberration
[3] Barbee, Troy W., Jr., "Nano-Laminates: A New Class of Materials for Aerospace Applications", Proceedings of the 2003 IEEE Aerospace Conference (Big Sky, Montana), IEEE, March 2003.
[4] Ealey, Mark A., "Large Optics in the 21st Century: A Transition from Discrete Manufacturing to Highly Integrated Techniques", Proceedings of the 2003 IEEE Aerospace Conference (Big Sky, Montana), IEEE, March 2003.
[5] David C. Redding, Fang Shi, Scott A. Basinger, David Cohen, Joseph J. Green, Andrew E. Lowman, Catherine M. Ohara, "Wavefront Control for Large Space Optics," IEEE Aerospace Conference (2003).
[6] Joseph J. Green, Benjamin Haber, Catherine M. Ohara, David C. Redding, Fang Shi, Mitchell Troy, J. Kent Wallace, "International Space Station Observatory," SPIE 7731-04 (2010).
[7] CERAFORM SiC
[8] T. W. Barbee, Jr., in "Synthetic Modulated Structures", edited by L. Chang and B. C. Giessen (Academic Press, New York, 1985) p. 313.
[9] T. J. Barbee, in "Physics, Fabrication and Applications of Multilayered Structures", edited by P. Dhez and C. Weisbach (Plenum Press, New York, 1988) p. 17.
[10] T. W. Barbee, Jr. and D. L. Keith: Synthesis of Metastable Materials by Sputter Deposition Techniques. Journal of Metals 32, 11. (1980).
[11] A. M. Hodge, Y. M. Wang and T. W. Barbee, Jr.: Large-scale production of nano-twinned, ultrafine-grained copper. Materials Science and Engineering a-Structural Materials Properties Microstructure and Processing 429, 272. (2006).
[12] Y. M. Wang, J. Li, A. V. Hamza and T. W. Barbee, Jr.: Ductile crystal line-amorphous nanolaminates. Proceedings of the National Academy of Sciences of the United States of America 104, 11155. (2007).
[13] T. W. Barbee, Jr., Sputtered layered synthetic microstructure (LSM) dipersion elements, in "Proceedings of the Topical Conference on Low Energy X-Ray Diagnostic" (Monterey, CA, 1981) p. 131.
[14] T. W. Barbee: Multilayers for X-Ray Optics. Optical Engineering 25, 898. (1986).
[15] A. B. C. Walker, T. W. Barbee, Jr., R. B. Hoover and J. F. Lindblom: Soft-X-Ray Images of the Solar Corona with a Normal-Incidence Cassegrain Multilayer Telescope. Science 241, 1781. (1988).
[16] C. J. Shute, B. D. Myers, S. Xie, T. W. Barbee, Jr., A. M. Hodge and J. R. Weertman: Microstructural stability during cyclic loading of multilayer copper/copper samples with nanoscale twinning. Scripta Materialia 60, 1073. (2009).
[17] David C. Redding, Gregory Hickey, G. Agnes, P. Eisenhardt, J.J. Green, J. Krist, L. Peterson, K. Stapelfeldt, W. Traub, S. Unwin, M. Werner, "Active Optics for a 16-Meter Advanced Technology Large Aperture Space Telescope," SPIE Astronomical Instrumentation Symposium, Marseilles, June 2008.
[18] C. Ohara, J. Faust, A. Lowman, J. Green, D. Redding, S. Basinger, D. Cohen, F. Shi, "Phase retrieval camera testing of the Ball Advanced Mirror System Demonstration," Proc. SPIE 5487 (2004).
[19] SHC
[20] Erkin Sidick, Joseph J. Green, Rhonda M. Morgan, Catherine M. Ohara, and David C. Redding, "Adaptive cross-correlation algorithm for extended scene Shack–Hartmann wavefront sensing," Optics Letters, Vol. 33, No. 3 (2008).
[21] Bikkans
[22] J. Green, S. Basinger, D. Cohen, A. Neissner, D. Redding, S. Shaklan and J. Trauger, "Demonstration of Extreme Wavefront Sensing Performance on the TPF High Contrast Imaging Testbed," Proc. SPIE 5170 (2003)
[23] MGS NTR.